Processing and Application of Ceramics 18 [1] (2024) 65–76
https://doi.org/10.2298/PAC2401065L

The influence of vanadium and titanium oxides in slag on the wetting and corrosion of dense Al_2O_3 ceramics

Zhaoyang Liu[1,2,*], Yuqing Gao[2], Songyang Pan[2], Ruinan Zhang[2], Wei Gao[2], Tianpeng Wen[1,2], Beiyue Ma[1,2,*], Jingkun Yu[2]

[1]*Key Laboratory for Ecological Metallurgy of Multimetallic Ores (Ministry of Education), Northeastern University, Shenyang, 110819, Liaoning, China*
[2]*School of Metallurgy, Northeastern University, Shenyang, 110819, Liaoning, China*

Received 19 November 2023; Received in revised form 6 February 2024; Accepted 5 March 2024

Abstract

The present study investigates the wetting and corrosion behaviour of slags on dense Al_2O_3 ceramics, focusing on the influence of varying vanadium- and titanium oxide content. Physicochemical properties of the slag were assessed by measuring wetting angles, heights and diameters of the molten slags on the alumina at different temperatures. Microscopic observations and elemental composition analysis were conducted on the interface between the corroded Al_2O_3 ceramics and the slags. Our findings demonstrated that the V_2O_3 addition in the slag leads to its oxidation to V_2O_5, which further reacts with Fe_2O_3 and MnO to form low melting point phases such as $FeVO_4$ and $MnVO_6$. Consequently, the melting point of the slag decreases significantly, resulting in a decreased wetting angle with the Al_2O_3 ceramics. The presence of unsaturated alumina in the slag leads to the dissolution of aluminium ions from the ceramics into the slag, which reacts with Fe_2O_3 and MnO to form spinel phases, contributing to material loss of the ceramics. Infiltration of the slag into the Al_2O_3 predominantly occurs through the alumina grain boundaries. Two types of infiltration are identified: one involving reactions with alumina to form low melting point phases like Fe_2O_3 and the other involving inherent low melting point phases such as $MnVO_6$. In contrast, the penetration of SiO_2 into the alumina substrate is limited. Additionally, the dissolution of Al_2O_3 into the slag creates pathways for further infiltration. This study highlights the significant influence of Ti and V content on the physicochemical properties of the slag and provides insight into the corrosion mechanism of Al_2O_3 ceramics by Ti and V containing slags.

Keywords: *dense Al_2O_3 ceramics, vanadium and titanium oxides, molten slag, corrosion, wettability*

I. Introduction

Wettability is a key property that describes the ability of a liquid to spread on a solid surface, and it is commonly characterized by the contact angle. This parameter is associated with the surface or interface free energies, as explained by Young's equation [1–3]. In the context of refractories, the wetting behaviour between refractories and molten slag has garnered significant attention due to its direct impact on slag corrosion resistance [4–6]. By controlling the contact angle between the liquid slag and the solid refractory, it is possible to not only reduce refractory consumption but also ensure the smooth operation and the quality of hot metals in iron- and steel-making processes [7,8]. In general, larger contact angles between refractories and slag indicate greater resistance against slag corrosion [9,10]. A classic example is the carbon-containing refractories, which exhibit excellent slag corrosion resistance due to the non-wettability of carbon materials by slags [11–14]. Several studies have investigated the wettability and corrosion of refractories by molten slags. Nakashima *et al.* [15] provided a brief review of contact angles observed between various refractories and molten slags, highlighting that most refractories tend to exhibit wetting by liquid slags, particularly in cases where both materials have a propensity for chemical reactions. Additionally, slags with higher FeO contents

* Corresponding author: tel: +86 13889230463
e-mail: *liuzhaoyang@smm.neu.edu.cn* (Z. Liu)
maby@smm.neu.edu.cn (B. Ma)

generally exhibit relatively lower contact angles. Chung *et al.* [16,17] studied the wetting, spreading and penetration phenomena of slags on spinel discs using the dispensed drop technique, suggesting that the spreading behaviour of slag is influenced by viscous forces. Furthermore, physical and chemical reactions occur at the interface between the solid and liquid phases, resulting in element migration where the dissolution reaction affects the rate of spreading.

Al_2O_3-based refractories are extensively utilized as main lining materials in high-temperature furnaces within the steel industry [18–20]. However, their direct contact with slag flux makes them susceptible to corrosion and degradation, thereby significantly impacting the safe and efficient production of the furnaces [21]. Corrosion products arising from this interaction can introduce harmful exogenous inclusions, which subsequently compromise the purity of the molten steel and the overall quality of steel products [22,23]. Consequently, it is essential to comprehensively investigate the corrosion behaviour of refractories subjected to steel-making slag. Numerous studies have been conducted to examine the corrosion of Al_2O_3 by slags, considering varying temperatures, slag compositions and rotational speeds [24–26]. However, there is an inconsistency in the results reported in the literature owing to the different experimental conditions and application contexts. Sarkar *et al.* [27], for instance, examined the interaction between FeO powders and pure Al_2O_3 refractory under flash iron-making conditions. Their findings demonstrated the formation of $FeAl_2O_4$ at the interface, wherein the Fe^{2+} and Al^{3+} cations engaged in reverse diffusion. The extent of diffusion predominantly relied on temperature and the effective diffusion coefficient. Similarly, Song *et al.* [28] and Pan *et al.* [29] investigated the corrosion behaviour of Al_2O_3 ceramics by FeO-CaO-SiO_2-MgO-Al_2O_3 converter and blast furnace primary slags, respectively. The results highlighted that with increasing temperature, the slags more readily wetted the Al_2O_3 discs. This corrosion phenomenon primarily resulted from favourable surface wettability and dissolution of Al3+ from the disc into the slag. Furthermore, Zhang *et al.* [30] focused on the dissolution of commercial tabular Al_2O_3 in FeO- and MnO-containing calcia-magnesia-alumina-silica (CMAS) slags. They posited that the lower alumina content in the slag and slower diffusion of silicon ions led to the formation of a $CaO \cdot 6\,Al_2O_3$ layer and a spinel layer predominantly composed of aluminium, iron, manganese and magnesium at the interface. In addition, in similar study the effect of Al_2O_3 amount on the structure of CaO-MgO-Al_2O_3-SiO_2 glass-ceramics prepared from stainless-steel slag was investigated by Zhang *et al.* [31].

Despite numerous investigations into the corrosion behaviour of Al_2O_3 in slags, the majority of previous studies have primarily focused on the CaO-SiO_2-Al_2O_3-MgO-FeO_t slag system [32,33]. It is worth noting that the depletion of high-quality iron ore resources in recent years has necessitated the increased utilization of replaceable iron ore in certain enterprises [34,35]. Consequently, this shift results in variations in the slag composition and causes corresponding changes in the corrosion behaviour of the refractories. A prime example of this scenario is the production of steel using vanadium-titanium magnetite (VTM) as the raw material through the blast-converter furnace process [36,37]. This process yields vanadium slag, characterized by elevated quantities of iron, vanadium, titanium and manganese oxides, but with lower CaO, Al_2O_3 and MgO contents [38]. The significant disparities in physicochemical properties between vanadium slag and traditional slag give rise to distinct corrosion mechanisms affecting refractories [39,40]. Practical experience has demonstrated that the lifespan of lining materials employed in VTM smelting is considerably shorter compared to traditional iron ore smelting practices. Hence, it is imperative to thoroughly examine the corrosion behaviour and underlying mechanisms between vanadium- and titanium-containing slag and refractories, providing robust insights necessary to prolong the longevity of refractory materials.

To the best of our knowledge, there is a paucity of literature exploring the wetting and corrosion behaviour between vanadium- and titanium-containing slag and Al_2O_3-based refractories. Consequently, this study aims to investigate the spreading and wetting process of slag on dense Al_2O_3 ceramics using the sessile drop method. The apparent morphology of the slag, including contact angle, height and diameter, was systematically characterized at different temperatures to discern the relationship between apparent morphology variations and the chemical composition of the slag. Additionally, microscopic morphology observation and phase analysis were employed to examine the Al_2O_3 ceramics following slag corrosion, thereby facilitating a comprehensive discussion of the corrosion mechanisms exerted by vanadium- and titanium-containing slag on dense Al_2O_3 ceramics.

II. Experimental

The Al_2O_3 ceramics utilized in this study were obtained from Jingwei Special Ceramics Co. Ltd. located in Taizhou, P.R. China and had a diameter of 20 mm and a thickness of 2 mm. It had an Al_2O_3 content exceeding 99% and an apparent porosity below 1%. Analytical grade SiO_2, FeC_2O_4, MnO, V_2O_3 and TiO_2 were procured from Sinopharm Chemical Reagent Co. Ltd.

Table 1. Chemical compositions of slags with different V_2O_3 and TiO_2 content (wt.%)

Sample	SiO_2	FeO	MnO	V_2O_3	TiO_2
V0T0	28.6	57.1	14.3	0	0
V0T10	25.7	51.4	12.9	0	10
V20T0	22.9	45.7	11.4	20	0
V20T10	20	40	10	20	10

in Shanghai, China. These chemicals were accurately mixed and pre-melted in an electric furnace at temperature of 1500 °C for 2 h. Subsequently, the mixture was allowed to cool and hydraulic machine was used to prepare cylindrical slags with diameter of 4 mm and thickness of 4 mm. The different slag samples used in this experiment had varying chemical compositions and labels, as detailed in Table 1, depending on the quantities of V_2O_3 and TiO_2 employed.

The wetting and spreading behaviour of slag on the surface of Al_2O_3 ceramics were investigated through *in situ* observations using a high-temperature wetting angle measurement instrument [41]. This instrument comprises a resistance furnace, a movable arm, a sample stage, and a high-definition camera, among other components. The dynamic wetting angles were utilized to evaluate the wetting and diffusion phenomena of the slag on the dense Al_2O_3 ceramics. The instrument was heated to 600 °C and maintained at this temperature. The pre-pressed slag samples were positioned at the centre of the dense Al_2O_3 ceramics and introduced into the resistance furnace using the movable arm. Subsequently, the temperature was gradually increased at a constant rate until it reached 1450 °C temperature. During this process, high-speed cameras captured images of the slight deformation of the slag, and relevant data such as temperature and time were recorded by a computer. Once the experiment was completed, the sample was carefully retrieved using the movable arm and allowed to cool to room temperature. Analysis of the obtained images provided valuable information on the wetting angle, diameter, and height of the slag.

The identical slag samples were subjected to compression and subsequently positioned at the central location of the dense Al_2O_3 ceramics. They were then introduced into a muffle furnace and maintained at a temperature of 1350 °C for 6 h. Following the cooling process, the resulting samples were embedded in resin and symmetrically divided into two parts along the wetting region. In order to prepare the sample surfaces for analysis, rough and precision grinding techniques were employed, followed by polishing with sandpaper and a velvet cloth. For microstructural examination and compositional analysis of the sample surfaces, scanning electron microscope (SEM) in conjunction with an energy-dispersive X-ray spectrometer (EDS) was employed. Additionally, the composition and valence states of the elements present in the samples were determined using X-ray photoelectron spectroscopy (XPS) with the use of Thermo Scientific ESCALAB 250Xi. To assess the apparent porosity of the Al_2O_3 ceramics, the Archimedes method was utilized.

III. Results and discussion

The wetting and spreading dynamics of molten slag on a dense Al_2O_3 ceramics were captured using a high-speed camera. In order to investigate the wetting behaviour of molten slag on Al_2O_3 ceramics, the heights and diameters of the molten slags, as well as the contact angle between the slags and the Al_2O_3 disc, were measured using ImageJ software. As the temperature gradually increased, the four different slags, each with varying V and Ti content, underwent melting and proceeded to wet the surface of the dense Al_2O_3 ceramics. However, noticeable disparities in the initial melting temperatures and wetting rates were observed, signifying differences in melting points and viscosities among the slags. Moreover, distinct variations were observed in the morphological changes exhibited by the molten slag during the melting process.

Figure 1a displays the changes in slag height during the wetting and spreading process. Except for the V20T10 slag, which consistently decreased in height with increasing temperature, the heights of other slags initially increased and then decreased. This suggests that the V20T10 slag undergoes continuous shrinkage during melting, while other slags initially expand before contracting. The addition of V and Ti oxides in the slag contributes to the reduction in slag height. The determination of the slag's melting point typically relies on the half-ball temperature, which is the temperature at which the slag height is halved [42]. As it can be seen in Fig. 1a, the melting points of the V0T0, V0T10, V20T0 and V20T10 slags are approximately 1394, 1360, 1296 and 1273 °C, respectively, indicating a decrease in melting point with the inclusion of V and Ti oxides. Furthermore, the temperature range associated with the melting interval, defined as five-sixths to one-third of the initial slag height (indicated by the light purple region in

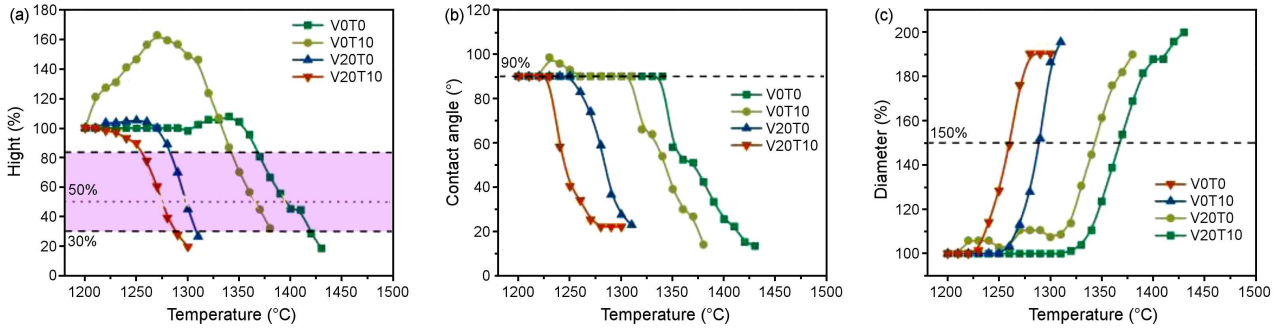

Figure 1. Height (a), contact angle (b), and diameter (c) of the slag on the dense Al_2O_3 ceramics

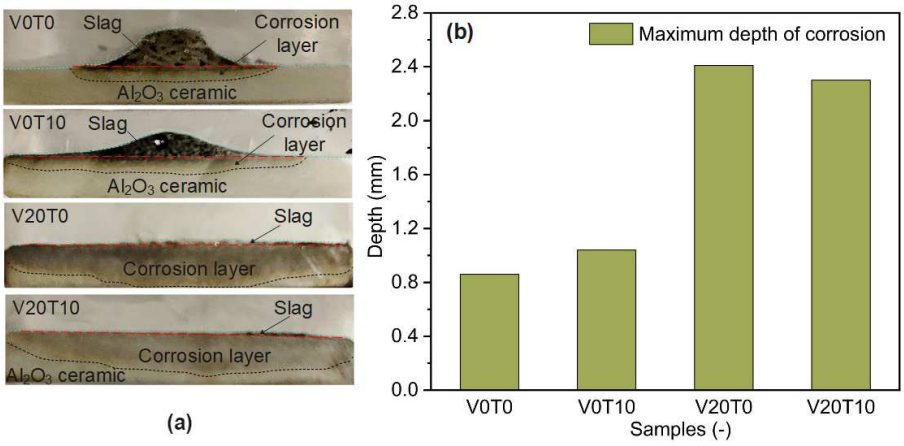

Figure 2. Maximum depth of the reaction zone in the dense Al_2O_3 ceramics with different slag compositions

Fig. 1a) [43], gradually shifts to lower temperatures with the addition of V and Ti oxides. For example, the melting interval for the V0T0 slag was 1255–1290 °C, while for the V20T10 slag it was 1370–1420 °C. It should be noted that the presence of a chemical reaction between the molten slag and the Al_2O_3 disc may influence the results of the melting point and melting interval. However, the short contact time between the slag and the Al_2O_3 disc suggests that the chemical reaction has minimal impact on the results. The changes in the contact angle between the molten slag with different V and Ti content and the dense Al_2O_3 disc with temperature are shown in Fig. 1b. The contact angle was measured from 1200 °C when the slag had not yet undergone melting, resulting in a contact angle of 90°. Contact angles of the V0T0, V20T0 and V20T10 slags decreased as the temperature increased, while the contact angle of the V0T10 slag initially exceeded 90° and gradually decreased thereafter. At the same temperature, the addition of V and Ti oxides resulted in a decrease in the contact angle between the slag and the dense Al_2O_3 disc. In Fig. 1c, the changes in slag diameter at different temperatures and with varying amounts of V_2O_3 and TiO_2 are depicted. The slag diameter increases as the temperature rises. The V0T0 slag demonstrates the widest temperature range for spreading, followed by the V0T10, V20T0 and V20T10 slags.

The examination of the vertical section of the samples after cooling is depicted in Fig. 2a. The irregular shape of the V0T0 slag indicates that the slag does not fully melt at the corrosion temperature, resulting in a smaller corrosion area beneath it. The periphery of the V0T10 slag on the Al_2O_3 disc appears relatively smooth, but the slag does not completely spread on the disc. This suggests that while the slag has undergone partial melting, its viscosity at this temperature remains comparatively high. This observation aligns well with the obtained melting point data (1360 °C) obtained through the droplet method. In contrast, the V20T0 and V20T10 slags exhibit extensive spreading over the alumina surfaces, with deeper corrosion compared to the V0T0 and V0T10 slags. Fig. 2b portrays the maximum corrosion depth of the dense Al_2O_3 disc resulting from slags with varying V and Ti contents. It is discernible that the addition of 10 wt.% TiO_2 to the slag marginally increases the corrosion depth compared to the slag without V_2O_3 and TiO_2. Conversely, the incorporation of 20 wt.% V_2O_3 significantly augments the corrosion depth, potentially penetrating through the dense Al_2O_3 disc. This outcome likely arises from the formation of low melting point phases between V in the slag and the disc, promoting the corrosive action of the slag on the disc. Moreover, when compared to the slag featuring only 20 wt.% V_2O_3, the corrosion depth slightly decreased with the addition of both 20 wt.% V_2O_3 and 10 wt.% TiO_2 in the slag.

In order to investigate the chemical composition of the V0T0 slag, XPS analysis was conducted, and the results are presented in Fig. 3. The C 1*s* peak at 284.8 eV was utilized for spectrum correction [44]. Figure 3a shows the overall spectrum of the V0T0 sample, revealing the presence of Fe, Si, Mn and O elements. Figure 3b presents the high-resolution Fe 2*p* spectrum, exhibiting peaks at 724.32 and 710.90 eV corresponding to Fe $2p_{1/2}$ and $2p_{3/2}$, respectively [45]. The energy difference between these peaks is approximately 13.60 eV, and their peak area ratio is approximately 2 : 1. Through the analysis of the energy position and shape characteristics of the Fe $2p_{3/2}$ peak, known as the shaken satellite peak, it can be inferred that iron is primarily in the Fe(III) state [46]. FeO resulting from the decomposition of FeC_2O_4 is completely oxidized to Fe_2O_3. Figure 3c demonstrates the Mn 2*p* spectrum, displaying peaks at 653.15 and 641.45 eV, corresponding to Mn $2p_{1/2}$ and $2p_{3/2}$, respectively. The energy difference between the spin-orbit split peaks is approximately 11.7 eV, and the peak area ratio (Mn $2p_{3/2}$: Mn $2p_{1/2}$) is roughly 2 : 1. The energy position and peak shape characteristics indicate that Mn(II) is the predominant manganese species [47].

To investigate the distribution and migration of elements during the reaction between slags and dense Al_2O_3, the four slag-contaminated dense Al_2O_3 specimens used in the wetting experiments were longitudinally sectioned. The cross-sections of the samples were then examined and analysed using SEM and EDS to

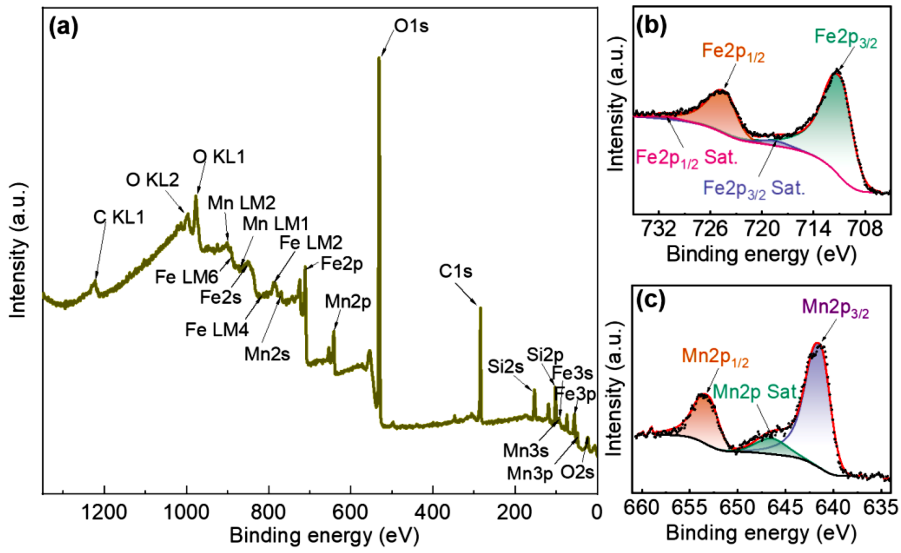

Figure 3. XPS results of V0T0 slag: a) survey, b) Fe 2*p* and c) Mn 2*p*

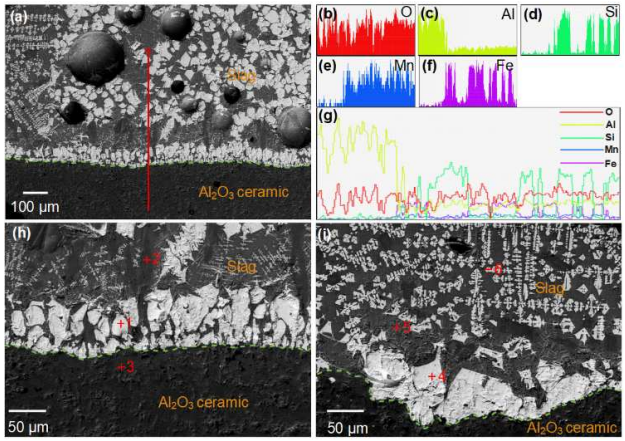

Figure 4. SEM images (a,h,i) and line scanning results (b-g) of the dense Al_2O_3 ceramics corroded by V0T0 slag

Table 2. EDS results of the selected points (Fig. 4) in the dense Al_2O_3 ceramics corroded by V0T0 slag (at.%)

Point	O	Al	Si	Mn	Fe	main phase
+1	62.19	9.74	-	4.26	23.82	spinel
+2	62.56	23.97	9.68	-	3.79	mullite
+3	61.13	36.13	-	-	2.75	Al_2O_3
+4	57.06	12.05	-	6.15	24.75	spinel
+5	69.74	8.02	17.31	2.26	2.67	silicate
+6	59.12	14.02	2.70	6.08	18.08	spinel

study their microstructure and composition. Figure 4 presents the micromorphology and element distribution in the dense Al_2O_3 samples after being corroded by the V0T0 slag. The SEM images displayed in Fig. 4a reveal the presence of grey-white crystalline phases precipitating from the liquid phase of the slag, particularly near the slag/Al_2O_3 interface on the slag side. No brightly coloured material was detected on the Al_2O_3 side. A closer examination of the line scan results presented in Figs. 4d-f demonstrates that Si, Mn and Fe elements from the slag successfully penetrate into the Al_2O_3 disc. However, the concentrations of these elements are notably higher on the slag side compared to the disc side, indicating that only a minimal amount of molten slag permeates into the interior of the Al_2O_3 disc. Conversely, the content of Al experiences a sudden decrease upon entering the slag side through the interface (Fig. 4c). The Al content remains relatively constant within the slag, indicating its distribution in both the crystalline and liquid phases. Table 2 records the elemental compositions of selected points through spot-EDS analysis. The presence of Al elements transferred from the dense Al_2O_3 ceramics to the slag is evident, contributing to the formation of crystalline phases (points +1, +4, and +6). Additionally, the V0T0 slag comprises mullite (+2) and silicate (+5). The composition of point +3 demonstrates the infiltration of Fe elements from the slag into the dense Al_2O_3 matrix through the pores.

Figure 5 illustrates the XPS results obtained for the V0T10 slag. The full survey spectrum is presented in Fig. 5a, revealing the presence of Fe, Si, Mn, Ti and O elements. The high-resolution spectra of Fe 2*p* and Mn 2*p*, depicted in Figs. 5b and 5c respectively, exhibit energy positions and shape characteristics similar to those observed in the V0T0 slag. Therefore, it can be deduced that Fe is predominantly in the Fe(III) state, while Mn is present primarily as Mn(II). Fig. 5d showcases the Ti 2*p* spectrum with peaks located at 463.93 and 458.31 eV, corresponding to Ti $2p_{1/2}$ and $2p_{3/2}$, respectively. The energy difference between the spin-orbit split peaks in the Ti 2*p* fine spectrum is approximately 5.54 eV, and the peak area ratio is approximately 2 : 1. Based on the energy position and peak shape characteristics of the Ti $2p_{3/2}$ peak, which is similar to the previously reported study [48], it can be inferred that the predominant Ti species is Ti(IV).

Similarly to the line scan results observed for the V0T0 slag, the line scan analysis of the V0T10 also reveals the presence of Fe, Si, Mn and Ti elements within

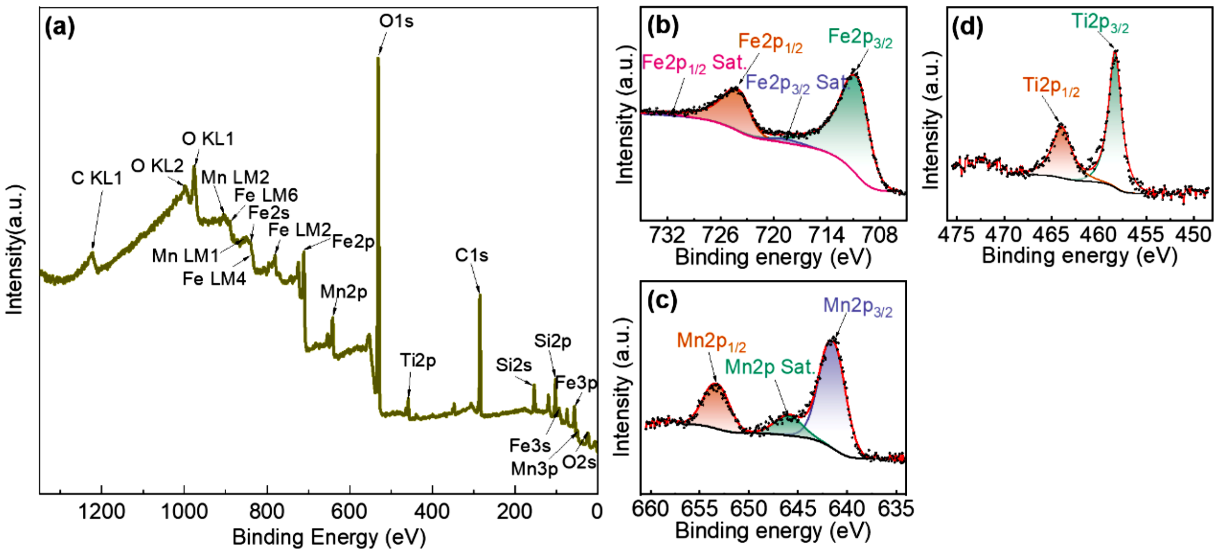

Figure 5. XPS results of V0T10 slag: a) survey, b) Fe 2*p*, c) Mn 2*p* and d) Ti 2*p*

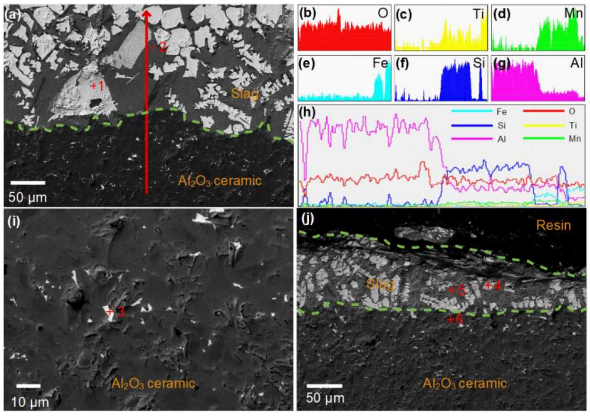

Figure 6. SEM images (a,i,j) and line scanning results (b-h) of the dense Al_2O_3 ceramics corroded by V0T10 slag

the dense Al_2O_3 matrix, while the Al element is predominantly concentrated on the slag side, as depicted in Fig. 6. However, a more pronounced corrosion phenomenon and an increased corrosion depth are observed in the interface region between the Ti-containing slag and the dense Al_2O_3 disc. A significant accumulation of white substances is evident at the boundaries of the alumina grains (Fig. 6i). To obtain a deeper understanding of the slag diffusion mechanism, we selected nine points near the V0T10 slag and dense Al_2O_3 interface for analysis. The phase composition of the slag during its reaction with the dense Al_2O_3 matrix has undergone a transformation. As shown in points +1 to +3, the slag predominantly consists of corundum and silicates. Moreover, points +4 to +6 indicate that Fe exhibits the highest propensity for penetration into the dense Al_2O_3 disc, followed by Ti and Mn. Throughout this process, reactions between Fe_2O_3, MnO, TiO_2 and Al_2O_3 occur, resulting in the formation of corundum phase. The interaction between TiO_2 and Al_2O_3 gives rise to the formation of a solid solution, which provides channels for the diffusion of elements like Fe and Mn into the dense Al_2O_3 matrix. The inclusion of TiO_2 lowers the slag's melting point, thereby facilitating the corrosion of the dense Al_2O_3 matrix.

The XPS analysis of the V20T0 slag was performed, and the results are illustrated in Fig. 7. The full survey spectrum of the V20T0 sample is presented in Fig. 7a, revealing the presence of Fe, Si, Mn, V and O elements. The high-resolution spectra of Fe 2*p* and Mn 2*p*, displayed in Figs. 7b and 7c respectively, indicate that iron primarily exists in the Fe(III) state, while the majority of the Mn species is Mn(II). Figure 7d features the high-resolution V 2*p* spectrum, with peaks at 522.24 and 514.53 eV corresponding to V $2p_{1/2}$ and $2p_{3/2}$, respectively, confirming the oxidation state of V^{3+}. Additionally, peaks located at 523.28 and 515.72 eV are attributed to V $2p_{1/2}$ and $2p_{3/2}$ of V^{4+}, and peaks at 524.44 and 517.08 eV correspond to V $2p_{1/2}$ and $2p_{3/2}$ of V^{5+} [49]. Through spectral analysis, the V^{3+}, V^{4+} and V^{5+} ratios were determined as 8.71%, 35.44% and 55.85%, respectively.

Table 3. EDS results of the selected points (Fig. 6) in the dense Al_2O_3 ceramics corroded by V0T10 slag (at.%)

Point	O	Al	Si	Ti	Mn	Fe	Main phase
+1	58.31	12.74	-	0.62	7.80	20.52	Spinel
+2	64.85	8.73	20.00	0.89	4.05	1.48	SiO_2, mullite
+3	70.47	2.87	-	4.14	2.44	20.08	Spinel
+4	63.48	5.40	-	3.53	4.49	23.10	Spinel
+5	68.09	9.41	17.62	1.00	2.93	0.95	SiO_2, mullite
+6	62.27	34.68	-	-	-	3.06	$(Al,Fe)_2O_{3ss}$

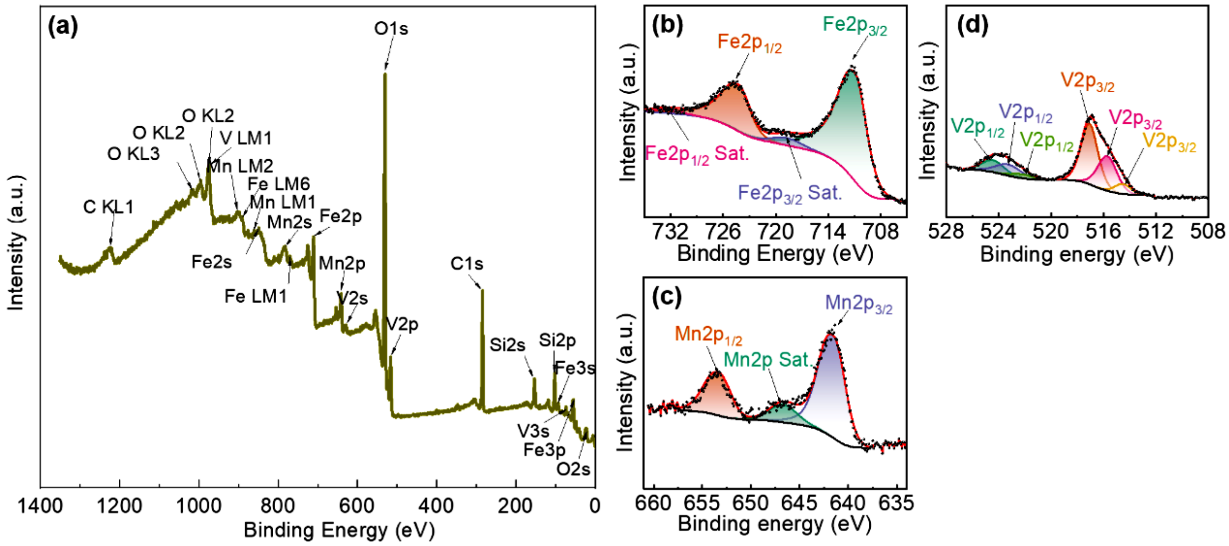

Figure 7. XPS results of V20T0 slag: a) survey, b) Fe 2*p*, c) Mn 2*p* and d) V 2*p*

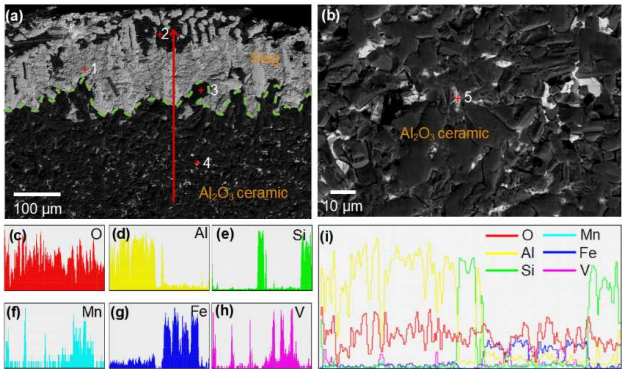

Figure 8. SEM images (a,b) and line scanning results (c-i) of the dense Al_2O_3 ceramics corroded by V20T0 slag

To gain insights into the mechanisms underlying the corrosion of the dense Al_2O_3 matrix by the V20T0 slag, comprehensive microstructural observations and elemental composition analyses were conducted at the reaction interface between the two materials. The line scan results depicted in Fig. 8 provide information regarding the distribution of key elements. Notably, compared to the corrosion caused by the V0T0 slag, the corrosion induced by the V20T0 slag was found to be more severe, characterized by the absence of a distinct reaction interface in the scanning images. This observation suggests vigorous diffusion taking place at the liquid-solid interface. From Fig. 8e to 8g, discernible diffusion of elements including Mn, Fe and V from the slag into the matrix is apparent. Conversely, the Al content demonstrates an inverse trend, indicating Al diffusion from the matrix into the slag. The incorporation of 20 wt.% V_2O_3 in the slag led to a decrease in the melting point. The XPS results shown in Fig. 7 indicate that a majority of the V_2O_3 underwent oxidation to V_2O_5 during the pre-melting process of the slag. It is reasonable to assume that in the subsequent wetting and erosion process, the remaining 3- and 4-valent vanadium species will also be oxidized to the 5-valent state. This oxidation of V_2O_3 to V_2O_5 results in the formation of certain low-melting-point phases, such as MnV_2O_6 (incongruent melting at 820 °C) [50] and $FeVO_4$ (incongruent melting at 840 °C) [51]. This phenomenon is evident from point +1 in Fig. 8. The heightened silicon content at points +2 and +3 indicates the presence of silicates within these specific regions. Analysis of points +4 and +5 in the inner region of the Al_2O_3 ceramics reveals the penetration of MnV_2O_6 and Fe_2O_3 phases from the slag into the ceramics, with the latter undergoing a reaction with Al_2O_3 to form solid solution phases.

XPS analysis was conducted on the V20T10 slag, and the results are presented in Fig. 9. Based on the energy positions and shapes of the peaks observed in Fe 2*p*, Mn 2*p* and Ti 2*p* spectra, it can be deduced that Fe predominantly exists in the Fe(III) state, Mn in the Mn(II) state and Ti in an unidentified state. Further examination of the energy positions and relative peak areas in the high-resolution V 2*p* spectrum, as depicted in Fig. 9d, reveals the presence of V in oxidation states of +3, +4 and +5, with respective ratios of 14.95%, 37.86% and 47.20%.

As illustrated in Fig. 10, the inner regions of the Al_2O_3 disc exhibited a white and bright appearance un-

Table 4. EDS results of the selected points (Fig. 8) in the dense Al_2O_3 ceramics corroded by V20T0 slag (at.%)

Point	O	Mg	Al	Si	V	Mn	Fe	Main phase
+1	61.32	-	2.12	-	18.78	8.51	9.27	$FeVO_4$, $Mn_2V_2O_7$
+2	64.03	-	1.25	29.74	2.27	1.01	1.70	SiO_2
+3	66.13	-	1.37	32.24	0.27	-	-	SiO_2
+4	68.72	-	7.96	2.18	0.52	0.74	19.90	$(Fe,Al)_2O_{3ss}$
+5	66.55	1.74	2.73	-	15.64	10.76	2.58	$Mn_2V_2O_6$, $FeVO_4$

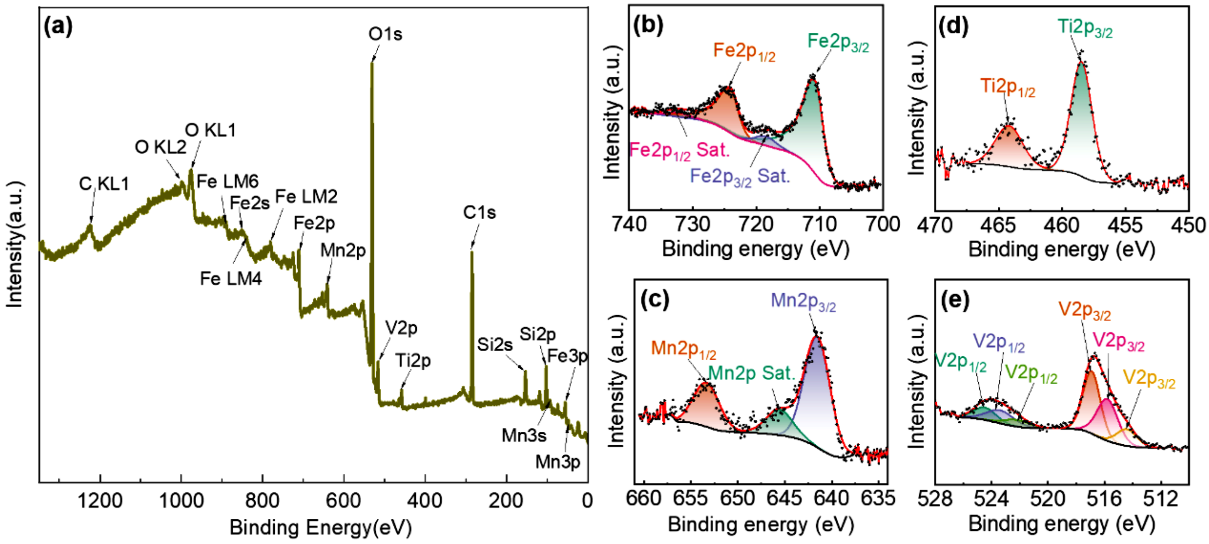

Figure 9. XPS results of V20T0 slag: a) survey, b) Fe 2*p*, c) Mn 2*p*, d) Ti 2*p* and e) V 2*p*

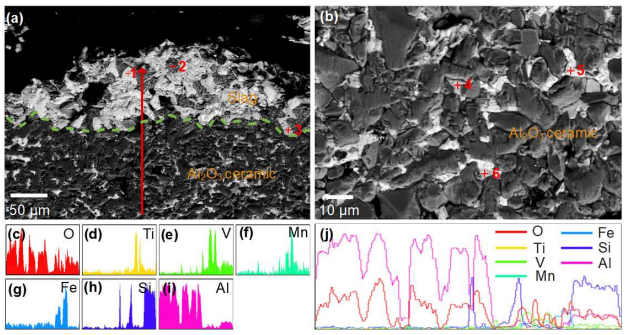

Figure 10. SEM images (a,b) and line scanning results (c-j) of the dense Al_2O_3 ceramics corroded by V20T10

der SEM analysis, indicating the replacement of these sections by high-concentration atomic species within the disc. This observation suggests that the dense Al_2O_3 matrix experienced severe corrosion by the V20T10 slag. The corrosion process involved both physical infiltration and chemical reaction dissolution, with the latter being considered the predominant pathway for infiltration. The line-scanning results reveal significant diffusion of elements such as Si, Fe, V, Mn and Ti from the slag into the Al_2O_3 ceramics, while the presence of Al in the slag side is also evident. Based on the elemental composition observed at point +1 (Fig. 10a), it can be deduced that the whitish crystalline phase present in the slag corresponds to Fe-rich corundum containing Al_2O_3 and TiO_2. Point +2 indicates the occurrence of a silicate phase, while points +3 and +4 correspond to the low melting point phases of $Mn_2V_2O_7$ and $FeVO_4$. Further inspection at points +5 and +6 reveals the formation of Fe-rich corundum and $Fe_{1.6}Al_{0.8}TiO_5$ phases.

The corrosion process of refractory materials by molten slag can be divided into two main aspects. Firstly, the penetration of molten slag occurs through pores, cracks and grain boundaries within the refractory material. This process is influenced by factors such as the porosity and pore size of the refractory as well as the melting point and viscosity of the slag [52]. Dissolution of the refractory also creates channels through which the slag can infiltrate. Secondly, the reaction between molten slag and the refractory material leads to the formation of low melting point compounds, resulting in the melting loss of refractory. This chemical reaction is dependent on the composition and flow state of the molten slag [53]. Extensive studies have shown that the properties of the slag significantly affect the corrosion of refractory materials [54–56]. In the present study, the addition of V_2O_3 and TiO_2 altered the performance of the slag, thereby impacting its corrosion process when in contact with the refractory.

Since the chosen Al_2O_3 ceramics in this study exhibited low porosity, around 0.25 ± 0.10%, its influence on corrosion was minimal. Consequently, the properties of the slag played a major role in the corrosion of the Al_2O_3 ceramics. The corrosion mechanism of the dense Al_2O_3 disc in the studied slags can be elucidated in the following way. At the experimental temperature of 1350 °C, the V0T0 and V0T10 slags were not com-

Table 5. EDS results of the selected points (Fig. 10) in the dense Al_2O_3 ceramics corroded by V20T10 slag

Point	O	Mg	Al	Si	Ti	V	Mn	Fe	Main phase
+1	61.27	-	4.69	-	2.75	0.63	1.76	28.91	corundum
+2	65.87	-	5.67	18.95	0.67	5.53	2.08	1.23	Silicate
+3	57.28	2.78	-	-	-	21.05	16.64	2.24	$Mn_2V_2O_7$, $FeVO_4$
+4	47.93	1.59	2.39	1.64	-	24.66	19.01	2.77	$Mn_2V_2O_7$, $FeVO_4$
+5	66.32	-	3.57	-	1.82	0.51	1.37	26.41	$(Fe,Al)_2O_{3ss}$
+6	72.20	-	5.86	-	7.39	1.27	0.75	12.53	$Fe_{1.6}Al_{0.8}TiO_5$

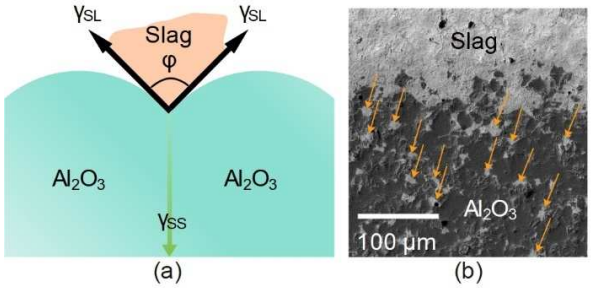

Figure 11. Schematic diagram (a) and SEM image (b) of the slag penetrating into the Al_2O_3 through grain boundary

pletely melted and contained a partially solid phase with high viscosity. As a result, the penetration of the slag into the interior of the dense Al_2O_3 disc was limited, resulting in less presence of slag within the disc. However, due to the insufficient amount of Al_2O_3 in the initial slag, aluminium ions in the disc diffused to the slag and underwent reactions to form compounds such as $(Al,Fe)_2O_3$ solid solution and mullite phase. This led to the degradation of the Al_2O_3 disc. Overall, the extent of corrosion caused by the V0T0 and V0T10 slags on the Al_2O_3 disc was relatively low.

Upon the addition of 20% V_2O_3 to the slag, V_2O_3 undergoes oxidation under low oxygen partial pressure conditions, forming V_2O_5. Further reactions of V_2O_5 with Fe_2O_3 and MnO in the slag result in the generation of low melting point phases like $FeVO_4$ and $MnVO_6$, which significantly decrease the melting point and viscosity of the slag. At the corrosion temperature, the slag evenly spreads over the surface of the Al_2O_3 disc. Previous studies have shown that the infiltration rate of the slag into the refractory increases as the slag viscosity decreases [57] (Eq. 1):

$$l = \sqrt{\frac{\sigma \cdot \cos\theta}{2\eta} \cdot r \cdot t} = k_t \sqrt{t} \tag{1}$$

where l is the erosion depth, t is the erosion time, r is the pore radius, θ is the wetting angle, η is the viscosity of slag, σ is the interfacial tension, k_t is the theoretical permeability coefficient. The V_2O_5-containing slag with lower viscosity enhances slag fluidity, facilitating penetration of the slag into the Al_2O_3 disc. Moreover, it accelerates mass transfer at the reaction interface, allowing for increased contact between the refractory components and the slag, ultimately leading to the formation of compounds and further exacerbating the disintegration of the disc [58]. Despite the apparent porosity of the Al_2O_3 disc being merely 0.25 ± 0.10%, molten slag can still penetrate into the interior through grain boundaries (Fig. 11). This can be explained by the relationship expressed in Eq. 2 [59], wherein the decrease in the interfacial energy between the solid and liquid phases promotes greater penetration of the slag into the brick sample:

$$\gamma_{SS} = 2\gamma_{SL} \cos\frac{\varphi}{2} \tag{2}$$

where γ_{SS} is the solid-solid interfacial energy and γ_{SL} is the solid-liquid interfacial tension and φ is the dihedral angle. Consequently, the microstructure and densification of the Al_2O_3 disc underwent changes and degradation.

Similar to the V0T0 and V0T10 slags, the V20T0 and V20T10 slags still did not reach the saturation point for alumina content. Consequently, Al_2O_3 can be dissolved into the slag due to the thermodynamic driving forces, represented by the Al_2O_3 concentration difference between the disc and the molten slag (the second Fick's Law, Eq. 3) [60]:

$$J = k(C_m - C_0) \tag{3}$$

where J is the mass transfer flux, k is the mass transfer coefficient of a substance, C_m is the substance content in the slag and C_0 is the content of substance in the matrix. Additionally, V_2O_5 may enhance the solubility of Al_2O_3 in the slag, facilitating direct dissolution of the disc. Therefore, the degree of slag-induced disc degradation increases with the addition of V_2O_5. The dissolution of detached Al_2O_3 grains into the slag creates pathways for slag penetration into the disc. This dissolution process alters the microstructure of the Al_2O_3 ceramics, leading to the direct corrosion of the disc. Typically, the rate-determining step of a refractory dissolution into slag at high temperatures involves mass diffusion or transport. However, line scanning results show no significant concentration gradient of Al element in the slag, indicating that its content is mainly determined by different

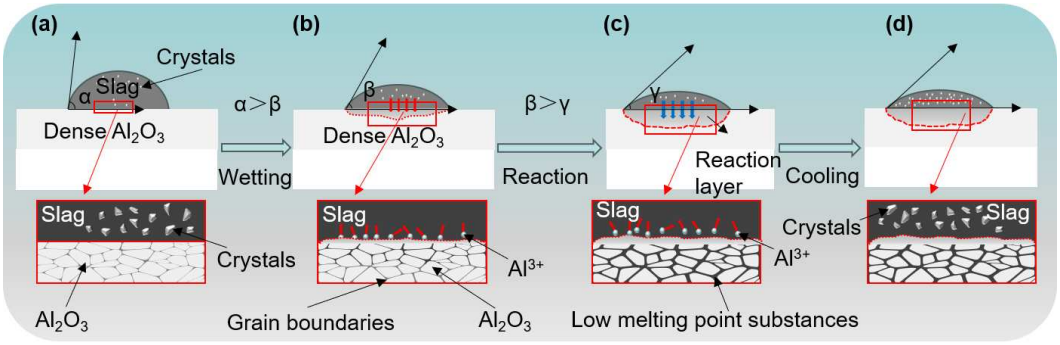

Figure 12. Schematic diagram of the corrosion process of dense Al_2O_3 ceramics by V and Ti containing slags

phases. Therefore, it is insufficient to determine the rate-controlling step of Al_2O_3 ceramics dissolution, calling for further investigation. Due to the combined effects of slag diffusion and alumina dissolution, the extent of slag corrosion deepens (Fig. 12).

IV. Conclusions

This study investigates the influence of Ti and V content on the wetting and erosion behaviour of slag on the dense Al_2O_3 ceramics. The wetting angle, height and diameter of the slag on the disc were measured at various temperatures to explore the impacts of Ti and V on the physicochemical properties of the slag. Microscopic observations of morphology and elemental composition analysis were conducted on the interface between the Al_2O_3 ceramics and the slag after erosion, aiming to elucidate the mechanism behind the corrosion of dense alumina discs by Ti- and V-containing slags. The key findings of this study are are the following:

1. V_2O_3, when added to the slag, readily oxidizes to V_2O_5. The resulting V_2O_5 reacts with FeO_3 and MnO in the slag, forming low melting point phases such as $FeVO_4$ and $MnVO_6$. Consequently, the melting point of the slag decreases significantly, along with a decrease in the wetting angle between the slag and the Al_2O_3 ceramics.
2. The concentration gradient of aluminium from the disc towards the slag leads to the dissolution of aluminium ions into the slag. These aluminium ions subsequently react with Fe_2O_3 and MnO, resulting in the formation of spinel phases. The migration of aluminium ions to the slag leads to the material loss of the ceramics.
3. The predominant infiltration pathway of the slag into the disc occurs through the grain boundaries of alumina. Two main types of infiltration can occur: one involving reactions with alumina to form low melting point phases, such as Fe_2O_3, and the other involving inherent low melting point phases, such as $MnVO_6$. In contrast, the penetration of SiO_2 into the alumina disc is relatively minor. Concurrently, the dissolution of Al_2O_3 into the slag creates pathways for the infiltration of the slag into the disc.

Acknowledgements: The authors would like to express their gratitude for the financial support from the National Natural Science Foundation of China (Grant No. 52004058) and the Fundamental Research Funds for the Central Universities (N2325014).

References

1. O. Jankovsky, E. Storti, G. Schmidt, S. Dudczig, Z. Sofer, C.G. Aneziris, "Unique wettability phenomenon of carbon-bonded alumina with advanced nanocoating", *Appl. Mater. Today*., **13** (2018) 24–31.
2. Q.H. Wang, G. He, S.X. Deng, J. Liu, J.T. Li, Y.W. Li, L.P. Pan, G.H. Liu, X.Y. Li, J.Q. Li, "Wettability and infiltration of Si drop on silica substrate containing α-Si_3N_4 coating: Influence of oxygen content in α-Si_3N_4 coating", *Ceram. Int.*, **46** (2020) 12695–12704.
3. Z.Y. Liu, J.K. Yu, X. Yang, E.D. Jin, L. Yuan, "Oxidation resistance and wetting behavior of MgO-C refractories: Effect of carbon content", *Materials*, **11** (2018) 883.
4. Y.M. Gao, H.C. Zhang, Q. Wang, G.Q. Li, "Effect of applied voltage on wetting and corrosion of corundum refractory by CaO-SiO_2-MgO molten slag", *Ceram. Int.*, **48** (2022) 9753–9764.
5. D.H. Ding, L.H. Lv, G.Q. Xiao, J.Y. Luo, Y. Ren, S.L. Yang, P. Yang, X. Hou, "Improved properties of low-carbon MgO-C refractories with the addition of multilayer graphene/$MgAl_2O_4$ composite powders", *Int. J. Appl. Ceram.*, **17** (2019) 645–656.
6. M.Q. Liu, J.T. Huang, Q.M. Xiong, Q.M. Xiong, S.Q. Wang, Z. Chen, X.B. Li, Q.W. Liu, S.W. Zhang, "Micro-nano carbon structures with platelet, glassy and tube-like morphologies", *Nanomaterials*, **9** (2019) 1242.
7. B.J. Monaghan, R.J. Longbottom, S.H. Zhang, "Wettability of CaO-SiO_2-MgO-Al_2O_3 liquid slag on solid Al_2O_3", *Metall. Mater. Trans. B*, **52** (2021) 4023–4032.
8. Y. Bin, X.W. Lv, S.L. Xiang, C.U. Bai, J.Q. Yin, "Wetting behavior of Al_2O_3 substrate by calcium ferrite series melts", *ISIJ Int.*, **55** (2015) 483–490.
9. S.M. Seo, D.S. Kim, Y.H. Paik, "Wetting characteristics of CaO-SiO_2-Al_2O_3 ternary slag on refractory oxides, Al_2O_3, SiO_2 and TiO_2", *Met. Mater.*, **7** (2001) 479–483.
10. B.J. Monaghan, S.H. Zhang, R.J. Longbottom, "Wettability of CaO-SiO_2-MgO-Al_2O_3 liquid slag on solid Al_2O_3", *Metall. Mater. Trans. B*, **52** (2021) 4023–4032.
11. Z.Y. Liu, J.K. Yu, X.N. Wang, P.C. Ma, W.B. G, J. Wen, S, Wei, X.F. Zhang, Z.G. Yan, T.P. Wen, L. Yuan, B.Y. Ma, "Comparative study of B_4C, $Mg_2B_2O_5$, and ZrB_2 powder additions on the mechanical properties, oxidation, and slag corrosion resistance of MgO-C refractories", *Ceram. Int.*, **48** (2022) 14117–14126.
12. Z.Y. Liu, J.K. Yu, S.J. Yue, D.B. Jia, E.D. Jin, B.Y. Ma, L. Yuan, "Effect of carbon content on the oxidation resistance and kinetics of MgO-C refractory with the addition of Al powder", *Ceram. Int.*, **46** (2020) 3091–3098.
13. D.H. Ding, X.C. Chong, G.Q. Xiao, L.H. Lv, C.K. Lei, J.Y. Luo, Y.F. Zang, "Combustion synthesis of $B_4C/Al_2O_3/C$ composite powders and their effects on properties of low carbon MgO-C refractories", *Ceram. Int.*, **45** (2019) 16433–16441.
14. P. Shen, H. Fujii, K. Nogi, "Wettability of some refractory materials by molten SiO_2-MnO-TiO_2-FeO_x slag", *Mater. Chem. Phys.*, **114** (2009) 681–686.
15. K. Nakashima, K. Mori, "Interfacial properties of liquid iron alloys and liquid slags relating to iron- and steel-making processes", *ISIJ Int.*, **32** (1992) 11–18.
16. T. Yoon, K. Lee, B. Lee, Y. Chung, "Wetting, spreading and penetration phenomena of slags on $MgAl_2O_4$ spinel refractories", *ISIJ Int.*, **57** (2017) 1327–1333.
17. S. Kim, K. Lee, Y. Chung, "Dissolutive wetting and spreading phenomena between Al_2O_3 substrate and CaO-Al_2O_3 liquid slags", *Metall. Mater. Trans. B*, **47** (2016) 1209–1216.
18. J.F. Chen, Y. Zhang, G.P. Liu, G.P Wei, Y. Zhao, W. Yan, N, Li, "Deterioration mechanism of Al_2O_3-MgO refractory castable in RH refining ladle", *Open Ceram.*, **16** (2023) 100467.
19. X.C. Chong, G.Q. Xiao, D.H. Ding, J.Y. Luo, P.Y. Yan, C. Zou, X. Hou, "Enhancement of oxidation resistance at

1000–1400 °C of low carbon Al_2O_3-C refractories with pre–synthesized SiC_{nw}/Al_2O_3", *Ceram. Int.*, **49** (2023) 31752–31762.
20. X.K. Tian, Y.L. Huang, L. Zhang, F. Zhao, Y.X. Chen, X.H. Liu, "Preparation of AlN-SiC bonded Al_2O_3-C refractory and its properties evolution after oxidation", *Ceram. Int.*, **50** (2023) 446–451.
21. Y.X. Luo, X. Wang, Z.L. Liu, C. Yu, C. Yu, C.J. Deng, J. Ding, "Strengthening mechanism and slag corrosion-resistance of low-carbon Al_2O_3-C refractories: Role of h-BN", *J. Mater. Res. Technol.*, **27** (2023) 3632–3643.
22. G. Li, H.Y. Tang, X.Y. Jiang, J.W. Liu, P. Lan, J.Q. Zhang, "Insights into ZrO_2- and Al_2O_3-based submerged entry nozzle clogging for the continuous casting of RE-treating sulfur resistant casing steel", *Ceram. Int.*, **48** (2022) 19732–19745.
23. J.L. Xiao, J.F. Chen, Y.Y. Li, Y.P. Cheng, M. Nath, Y. Zhang, L.J. Zheng, S.W. Zhang, N. Li, "Corrosion mechanism of cement-bonded Al_2O_3-$MgAl_2O_4$ pre-cast castables in contact with molten steel and slag", *Ceram. Int.*, **48** (2022) 5168–5173.
24. H.Y. Tang, G.H. Wu, Y. Wang, J.S. Li, P. Lan, J.Q. Zhang, "Comparative evaluation investigation of slag corrosion on Al_2O_3 and $MgOAl_2O_3$ refractories via experiments and thermodynamic simulations", *Ceram. Int.*, **43** (2017) 16502–16511.
25. Y.F. Peng, A. Huang, S.H. Li, S.H. Li, X.Y Chen, H.Z. Gu, "Radical reaction-induced turing pattern corrosion of alumina refractory ceramics with CaO-Al_2O_3-SiO_2-MgO slags", *J. Eur. Ceram. Soc.*, **43** (2023) 166–172.
26. J.Q. Song, Y.J. Liu, X.M. Lu, Z.X. You, "Corrosion behavior of Al_2O_3 substrate by SiO_2-MgO-FeO-CaO-Al_2O_3 slag", *J. Mater. Res. Technol.*, **9** (2020) 314–321.
27. R. Sarkar, H.Y. Sohn, "Interaction of ferrous oxide with alumina refractory under flash ironmaking conditions", *Ceram. Int.*, **45** (2019) 15417–15428.
28. J. Song, Y. Liu, X. Lu, Z.X. You, "Corrosion behavior of Al_2O_3 substrate by SiO_2-MgO-FeO-CaO-Al_2O_3 slag", *J. Mater. Res. Technol.*, **9** (2019) 314–321.
29. X.Y. Pan, F.M. Shen, Q.J. Gao, X. Jiang, H.Y. Zheng, "Effect of erosion behavior of FeO-CaO-SiO_2-MgO-Al_2O_3 blast furnace primary slag on Al_2O_3 substrate", *Crystals*, **11** (2021) 957.
30. S.W. Zhang, H.R. Rezaie, H. Sarpoolaky, W.E. Lee, "Alumina dissolution into silicate slag", *J. Eur. Ceram. Soc.*, **83** (2000) 897–903.
31. C.B. Zhang, Z.F. Tong, C.C. Xu, J.X. Wang, Z.H. Jia, "Effect of Al_2O_3 on migration and distribution of chromium and chromium fixation effect in stainless-steel slag glass-ceramics", *Process. Appl. Ceram.*, **17** (2023) 70–80.
32. F.J. Guo, Z.C. He, L Liu, J. Li, Y.D. Huang, "High-strength and corrosion-resistant Al_2O_3 ceramics with excellent closed-cell structure", *Ceram. Int.*, **48** (2022) 33160–33166.
33. G.J. Chen, S.P. He, Q. Wang, "Dissolution behavior of Al_2O_3 into tundish slag for high-Al steel", *J. Mater. Res. Technol.*, **9** (2020) 11311–11318.
34. Y.K. Li, S.Q. Li, X. Zhao, X.D. Pan, P.H. Guo, "Separation and purification of high-purity quartz from high-silicon iron ore tailing: An innovative strategy for comprehensive utilization of tailings resources", *Process Saf. Environ. Prot.*, **169** (2023) 142–148.
35. S.K. Roy, D. Nayak, S.S. Rath, "A review on the enrichment of iron values of low–grade Iron ore resources using reduction roasting–magnetic separation", *Powder Technol.*, **367** (2020) 796–808.
36. Y.F. Guo, K. Liu, F. Chen, S. Wang, L.Z. Yang, D.Y. Li, Y. Zheng, "Effect of high-pressure grinding rolls pretreatment on the preparation of vanadium-titanium magnetite pellets", *J. Mater. Res. Technol.*, **23** (2023) 2479–2490.
37. G.J. Cheng, L.J. Li, X.X. Xue, H. Yang, W.J. Zhang, R.G. Bai, "Effects of extracted-vanadium residue and MgO on the basic sintering characteristics of high-chromium vanadium-titanium magnetite", *J. Mater. Res. Technol.*, **17** (2022) 2657–2669.
38. Y.R. An, B.Z. Ma, X. Li, Y.Q. Chen, C.Y. Wang, B.H. Wang, M.L. Gao, G.S. Feng, "A review on the roasting-assisted leaching and recovery of V from vanadium slag", *Process Saf. Environ. Prot.*, **173** (2023) 263–276.
39. G.E. Wang, Y. Wang, B. Xie, X.S. Li, X. Guo, X.J. Li, "Effects of oxides contents in vanadium slag on corrosion mechanism of MgO-C bricks, *J. Iron Steel Res. Int.*, **19** (2012) 36–42.
40. B.Q. Han, C.M. Ke, Y.W. Wei, W. Yan, C.M. Wang, F.Y. Chen, N. Li, "Degradation of MgO-C refractories corroded by SiO_2-Fe_2O_3-V_2O_5-TiO_2-MnO-MgO slag", *Ceram. Int.*, **41** (2015) 10966–10973.
41. Z.Y. Liu, L. Yuan, E.D. Jin, X. Yang, J.K. Yu, "Wetting, spreading and corrosion behavior of molten slag on dense MgO and MgO-C refractory", *Ceram. Int.*, **45** (2019) 718–724.
42. H. Wang, G. Li, B. Li, X.J. Zhang, Y.Q. Yan, "Effect of B_2O_3 on melting temperature of CaO-based ladle refining slag", *J. Iron Steel Res. Int.*, **17** (2010) 18–22.
43. P. Shen, L.F. Zhang, Y. Wang, S. Sridhar, Q.Q. Wang, "Wettability between molten slag and dolomitic refractory", *Ceram. Int.*, **42** (2016) 16040–16048.
44. S.A. Abdullah, M.Z. Sahdan, N. Nafarizal, Z. Embong, C.H. Rohaida, F. Adriyanto, "Influence of substrate annealing on inducing Ti^{3+} and oxygen vacancy in TiO_2 thin films deposited via RF magnetron sputtering", *Appl. Surf. Sci.*, **462** (2018) 575–582.
45. A.P. Grosvenor, B.A. Kobe, M.C. Biesinger, N.S. McIntyre, "Investigation of multiplet splitting of Fe 2p XPS spectra and bonding in iron compounds", *Surf. Interface Anal.*, **36** (2004) 1564–1574.
46. M. Mullet, Y. Guillemin, C. Ruby, "Oxidation and deprotonation of synthetic Fe^{II}–Fe^{III} (oxy)hydroxycarbonate green rust: an X-ray photoelectron study", *J. Solid State Chem.*, **181** (2008) 81–89.
47. M.C. Biesinger, B.P. Payne, A.P. Grosvenor, L.W.M. Lau, A.R. Gerson, R.St.C. Smart, "Resolving surface chemical states in XPS analysis of first row transition metals, oxides and hydroxides: Cr, Mn, Fe, Co and Ni", *Appl. Surf. Sci.*, **257** (2011) 2717–2730.
48. S.A. Abdullah, M.Z. Sandan, N. Nayan, Z. Embong, C.R.C. Hak, F. Adriyanto, "Neutron beam interaction with rutile TiO_2 single crystal (111): Raman and XPS study on Ti^{3+}-oxygen vacancy formation", *Mater. Lett.*, **263** (2020) 127143.
49. J. Mendialdua, R. Casanova, Y. Barbaux, "XPS studies of V_2O_5, V_6O_{13}, VO_2 and V_2O_3", *J. Electron Spectros. Relat. Phenomena*, **71** (1995) 249–261.
50. L.L. Surat, V.D. Zhuravlev, Y.A. Velikodnyi, "Phase relations in the CoO-MnO-V_2O_5 system", *Russ. J. Inorg. Chem.*, **43** (1998) 520–522.

51. T. Jantzen, E. Yazhenskikh, K. Hack, M. Baben, G.X. Wu, M. Müller, "Addition of V_2O_5 and V_2O_3 to the CaO-FeO-Fe_2O_3-MgO-SiO_2 database for vanadium distribution and viscosity calculations", *Calphad*, **74** (2021) 102284.
52. Y.K. Zhang, L.E. Sun, Y. Lei, W.H. Ma, Z.H. Li, "Corrosion behavior of carbon, Al_2O_3, and MgO refractories during the preparation of a Ti-Si-Al alloy via the aluminothermic reduction of a Ti-bearing blast-furnace slag", *Ceram. Int.*, **47** (2021) 18044–18052.
53. Y.M. Gao, H.C. Zhang, P.W. Liu, Q. Wang, G.Q. Li, "Effect of MgO on wetting and corrosion behaviour of corundum substrate by CaO-SiO_2-MgO(-Al_2O_3) slags", *Ironmak. Steelmak.*, **50** [11] (2023) 1528–1538.
54. H.R. Zhang, L.G. Chen, G.Z. Gao, Q.L. Jia, P.Y. Xu, C.L. Ma, "Microstructure, mechanical property and slag corrosion resistance of (Al, Cr)$_2O_3$-Mg(Al,Cr)$_2O_4$-Ca(Al,Cr)$_{12}O_{19}$ composite refractory using alumina-chromia slag", *J. Eur. Ceram. Soc.*, **44** (2024) 557–566.
55. L. Zhang, A. Malfliet, B. Blanpain, M.X. Guo, "In situ electrical conductivity measurement by using confocal scanning laser microscopy", *Metall. Mater. Trans. B*, **52** (2021) 2563–2572.
56. L. Zhang, A. Malfliet, B. Blanpain, M.X. Guo, "Understanding the relationship between slag crystallization behaviour and electrical conductivity under isothermal conditions for online slag solidification monitoring in slag recycling", *Resour. Conserv. Recycl.*, **182** (2022) 106319.
57. L. Zhu, C.Y. Liu, C.M. Du, F.X. Huang, Y.L. Sun, Y. Jia, Y.F. Wang, B.Y. Ma, "Dissolution behavior of spent MgO-C refractory in the CaO-SiO_2-FeO slag system as a steelmaking flux", *Ceram. Int.*, **49** (2023) 24931–24940.
58. S.H. Li, A. Huang, H.Z. Gu, R.F. Wang, Y.S. Zou, L.P. Fu, "Corrosion resistance and anti-reaction mechanism of Al_2O_3-based refractory ceramic under weak static magnetic field", *J. Eur. Ceram. Soc.*, **105** (2022) 2869–2877.
59. W.E. Lee, S. Zhang, "Melt corrosion of oxide and oxide-carbon refractories", *Int. Mater. Rev.*, **44** (2013) 77–104.
60. P. Li, M. Zhang, Z.B. Wang, S. Seetharaman, "BF slag resistance of β-$Si_3Al_3O_3N_5$ material derived from Al salt cake", *J. Eur. Ceram. Soc.*, **35** (2015) 1307–1315.